

# 1    A neural network trained by 3D printed biomimetic cochleae provides 2    clinical informatics for cochlear implant patients

3    Iek Man Lei<sup>1,2</sup>, Chen Jiang<sup>3,1</sup>, Chon Lok Lei<sup>4</sup>, Simone Rosalie de Rijk<sup>3</sup>, Yu Chuen Tam<sup>5</sup>, Michael  
4    P.F. Sutcliffe<sup>1</sup>, George G. Malliaras<sup>1</sup>, Manohar Bance<sup>3,\*</sup>, Yan Yan Shery Huang<sup>1,2,\*,#</sup>

5    <sup>1</sup>*Department of Engineering, University of Cambridge, United Kingdom*

6    <sup>2</sup>*The Nanoscience Centre, University of Cambridge, United Kingdom*

7    <sup>3</sup>*Department of Clinical Neurosciences, University of Cambridge, United Kingdom*

8    <sup>4</sup>*Department of Computer Science, University of Oxford, United Kingdom*

9    <sup>5</sup>*Emmeline Centre for Hearing Implants, Addenbrookes Hospital, Cambridge, United Kingdom*

10   \*Corresponding authors: mlb59@cam.ac.uk, yysh2@cam.ac.uk

11   #Lead contact: yysh2@cam.ac.uk

12

## 13   **Abstract**

14   Cochlear implants (CIs) restore hearing in patients with severe to profound deafness by  
15   delivering electrical stimuli inside the cochlea. The high electrical conductivity inside the  
16   cochlea, however, causes the electrical stimulus to spread, reducing speech comprehension.

17   Understanding the stimulus spread in an individual patient is hampered by the poor  
18   accessibility of the inner ear and by the lack of suitable *in vitro* or *in vivo* models. Here, we

19   report on the development of a neural network model that is informed by measurements in  
20   3D printed biomimetic cochleae with realistic conductivity and anatomy. Using four

21   geometric features captured in patients' pre-operative CT scans, the model can reconstruct  
22   patients' clinical electric field imaging (EFI) profiles arising from off-stimulation positions

23   with a 90% mean accuracy ( $n=6$ ). Moreover, the model informs the stereotypical cochlear.  
NOTE: This preprint reports new research that has not been certified by peer review and should not be used to guide clinical practice.

24 geometries prone to stimulus spread and replicates the uncommon clinical occurrence of the  
25 ‘mid-dip’ EFI profiles. This work enables on-demand printing of patient-relevant cochlear  
26 models for CI testing, and directly reveals individual patient’s *in vivo* cochlear tissue  
27 resistivity (0.6 – 15.9kΩcm,  $n=16$ ) by CI telemetry.

28

29 **Introduction**

30 The use of prosthetic medical electronic implants and bioelectronic devices has been  
31 increasing rapidly, and is anticipated to form a new era of medicine<sup>1,2</sup>. By delivering local  
32 electrical stimuli to tissues, these electronic implants restore lost electrical functions in tissues  
33 or nerves, or modulate signalling patterns for therapeutic outcomes<sup>2,3</sup>. Cochlear implants  
34 (CIs) are by far the most widely used neuromodulation electronic implants, with well over  
35 500,000 CIs having been implanted worldwide<sup>4</sup>, and their prevalence is only expected to  
36 grow more rapidly with the projected increase in the elderly population<sup>1</sup>. Bypassing the  
37 malfunctioning peripheral auditory mechanisms, the CI electrode array is designed to restore  
38 sound perception, and preserves the tonotopic response of the cochlea by delivering  
39 programmed stimulation at localised regions of the cochlear lumen; this in turn stimulates  
40 separate auditory neural elements<sup>5,6</sup> (Fig.1a), with lower sound frequencies represented  
41 apically and higher frequencies basally.

42

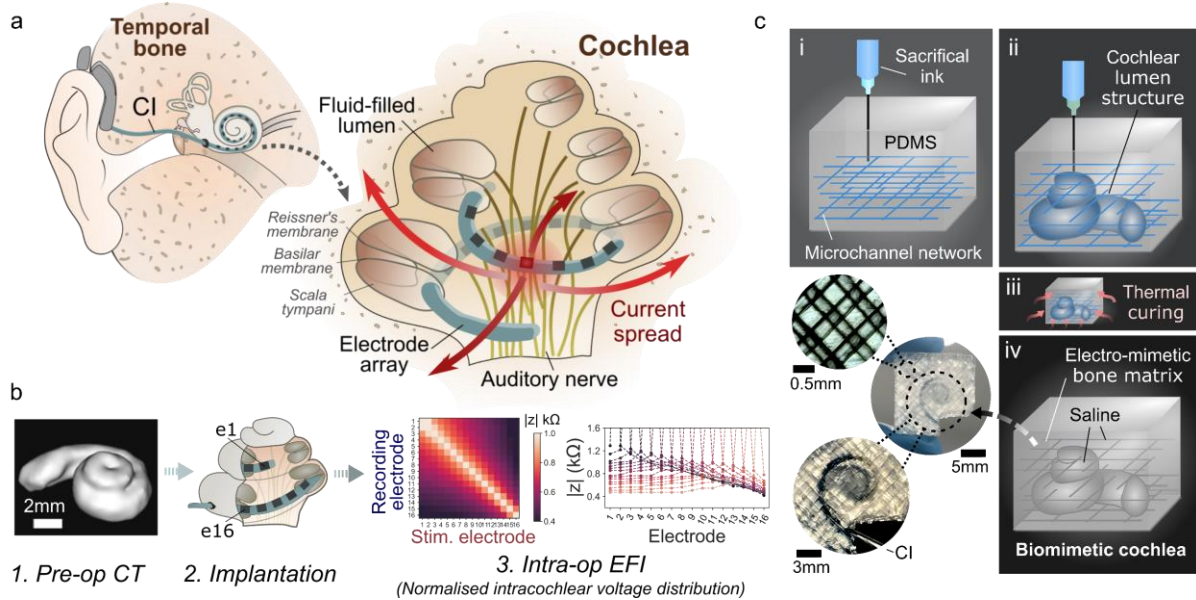
43

44

45

46

47 **Fig.1: Embedded 3D printing of biomimetic cochleae for reproducing the CI stimulus**  
48 **spread characteristics.**



49  
50 **a**, Schematic of the auditory system and the cochlea with a CI implanted. The ‘current  
51 spread’ problem induced by a stimulated electrode of the CI electrode array is indicated. **b**,  
52 Schematic of the routine CI assessment process; **1**. Routine pre-operative CT scan of a  
53 patient’s cochlea, which typically only has a resolution to reveal the ensemble spiral-shaped  
54 cavity of a cochlea; **2**. Implantation of the electrode array of a CI in the scala tympani of the  
55 cochlea; **3**. Acquisition of an EFI (electric field imaging) profile, which is derived from  
56 recording the induced intracochlear voltage  $V$  measured at each electrode upon injecting  
57 consecutive current pulses at each electrode in the array. The voltage measurements are then  
58 converted to transimpedance magnitude  $|z|$  by normalising the voltage  $V$  with the stimulation  
59 current impulse  $I_{stim}$  ( $|z| = V / I_{stim}$ ). The off-stimulation (off-diagonal) measurements in the  
60 EFI present information about the tissue impedance<sup>9</sup>. **c**, Schematic of the embedded 3D  
61 printing strategy to produce the electro-mimetic bone matrices and the biomimetic cochleae.

62  
63 A major limitation of today’s electronic implants is their imprecise control of the  
64 administered stimulus, arising from the intrinsic conductive nature of biological tissues, and  
65 particularly of the biological fluids in the inner ear<sup>4,5,7-9</sup>. This limitation is well exemplified  
66 by the ‘current spread’ problem of CIs, where the uncontrolled spread of electrical stimulus  
67 leads to off-target excitation of the neighbouring auditory nerves (thus causing a mismatch or  
68 ‘smeared’ representation in the perceived sound from that intended)<sup>4,9</sup> (Fig.1a). Cochlear

69 anatomy, tissue conductivity, and implant positioning are suggested to be the primary patient-  
70 specific factors controlling the intracochlear voltage distribution induced by CIs<sup>9–12</sup>. In  
71 particular, cochlear anatomy (in terms of size and shape) is variable, with different levels of  
72 volumetric conductance of cochlear fluids affecting the intracochlear voltage that results from  
73 stimulation. Moreover, pathophysiological conditions could affect electrical conductivity of  
74 the cochlear bony walls, and thus CI induced electric fields<sup>13</sup>. As the cochlea is embedded  
75 deep inside the temporal bone and has a complex anatomy, electrical characteristics are  
76 difficult to quantify in a living subject. As a result, a model that deciphers how the biologic  
77 characteristics of a patient's cochlea affect the stimulus spread would be a valuable tool for  
78 predicting and optimizing the stimulus signals that ultimately result in better sound  
79 perception and speech recognition. It may also provide insights into factors controlling the  
80 large variation in patient-specific CI performance.

81  
82 Although various physical and computational models have been developed for CI  
83 testing<sup>9,12,14–16</sup>, they are incomplete in evaluating the stimulus spread in human cochleae.  
84 Animal models are well-established for *in vivo* CI testing, but due to the drastic differences  
85 between the cochlear anatomies of humans and animals<sup>17</sup>, very incomplete insights into  
86 human responses are obtained<sup>1,3</sup>. Though human cadavers can provide anatomical fidelity,  
87 they are limited in supply and have altered electrical properties due to preservation and post-  
88 mortem changes<sup>18</sup>. *In silico* approaches, such as finite element modelling (FEM), can  
89 overcome ethical, sample availability and cost issues<sup>19</sup>. However, existing FEM modelling is  
90 limited by several factors, including scant knowledge of the electrical properties of live  
91 human cochleae tissues to fit different *in vivo* cases<sup>20</sup>, the inability to capture patient-  
92 dependent anatomical-guided CI positioning, and the under-determined boundary  
93 conditions<sup>14</sup>.

94 To establish a robust modelling framework for interpreting clinical CI testing data, we  
95 created a library of 3D printed cochlear models ( $n=82$ ) which captures the diverse geometry  
96 of the human cochlear lumen along with a spectrum of bone tissue resistivities within the  
97 reported range obtained from *in vivo* human studies. Supplementary Video 1 shows CT scans  
98 of exemplar 3D printed biomimetic cochleae. Using these models, a broad spectrum of  
99 clinically representative electric field imaging (EFI) profiles (normalised intracochlear  
100 voltage distribution along the CI electrode array) was acquired by varying the model electro-  
101 anatomical characteristics. Then, by inputting EFI profiles from the biomimetic cochleae as  
102 the training dataset, we establish a neural network model termed 3PNN (3D printing and  
103 neural network co-modelling), which provides powerful clinical informatics such as  
104 deciphering patient-specific attributes of CI current spreads, and extracting patient-dependent  
105 cochlear tissue resistivity.

106

## 107 **Results**

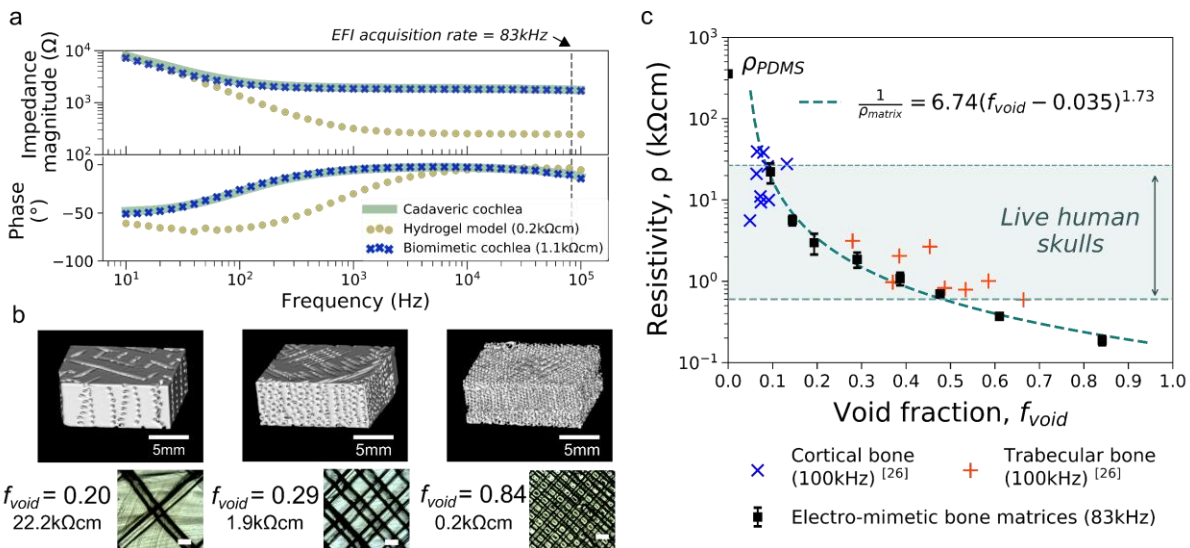
### 108 **Designable electro-mimetic bone matrices**

109 The human cochlea is a spiral-shaped hollow organ embedded in the temporal bone (Fig.1a).  
110 Since there were no established reports of *in vivo* cochlear tissue conductivities, our first goal  
111 was to establish a printable material system that could emulate the range of reported bone  
112 tissue conductivities (thereafter, termed electro-mimetic bone matrix). *In vivo* human studies  
113 during surgery estimated that the electrical resistivities of human skulls vary widely between  
114 0.6 to 26.6 kΩcm, depending on the site, composition, age and porosity<sup>21–25</sup> (Supplementary  
115 Fig.1a-b).

116

117 To reproduce the mesoscale electrical properties of bone, we take inspiration from the micro-  
118 architecture of bones, which consists of conductive fluid-filled interconnected pores  
119 surrounded by a poorly conductive mineralised phase<sup>26</sup>. Thus, we structured an electro-  
120 mimetic bone matrix that exhibits interconnected saline-filled channels inside a crosslinked  
121 PDMS (polydimethylsiloxane) elastomer. The interconnected channels were created by  
122 embedded printing a Pluronic F127 sacrificial ink in pre-crosslinked PDMS (Fig.1c,  
123 Supplementary Video 2), permitting flexible and precise tuning of the void density and,  
124 therefore, the resistivity of the electro-mimetic bone matrices (Supplementary Fig.2).  
125 Comparing our printing method with stereolithography, Pluronic F127 can be easily removed  
126 after printing<sup>27</sup> and further enhances the wettability of PDMS due to its amphiphilic nature.  
127 The channels were then filled with a physiological saline, which we hypothesise is important  
128 to emulate the electrical impedance properties of bone tissues, as pores in bone would  
129 normally be wet with extracellular fluids. The electrochemical impedance spectroscopy (EIS)  
130 measurements in Fig.2a and Supplementary Fig.3 show that an electro-mimetic bone matrix  
131 can be designed to exhibit impedance properties matching those of a human cadaveric  
132 cochlear bone, for the operating frequencies of CIs (i.e.  $f=1\text{-}100\text{ kHz}$ ). By varying the void  
133 fraction in the electro-mimetic bone matrix from 20% to 84%, the resistivity of the matrix  
134 can be tuned from 0.2 to 22 kΩcm (Fig.2b), covering almost the entire reported resistivity  
135 range of live human skull tissues<sup>21-25</sup> (0.6 – 26.6 kΩcm, Fig.2c).  
136  
137  
138  
139  
140  
141

142 **Fig.2: Electrical properties of electro-mimetic bone matrices.**



143

144 **a**, Bode plot showing the impedance properties of a cadaveric cochlea, and 3D printed  
145 cochlear models made of an electro-mimetic bone matrix and a hydrogel. **b**, Micro-CT  
146 reconstructed images (top) and optical microscopic images (bottom) of the electro-mimetic  
147 bone matrices at different volumetric void fractions ( $f_{void}$ ). Scale bar of the optical  
148 microscopic images = 500 $\mu$ m. The resistivities of the matrices were measured at 83kHz, the  
149 EFI acquisition rate used in this study<sup>28</sup>. **c**, Resistivity of the electro-mimetic bone matrices ( $n$   
150  $\geq 3$ ) as a function of  $f_{void}$ , compared to the reported resistivities of bovine cortical and  
151 trabecular bones<sup>26</sup>. The relationship between the resistivity of the electro-mimetic bone  
152 matrix and  $f_{void}$  is well-described by a percolation equation of a conductor-insulator  
153 composite<sup>29</sup> (Supplementary Fig.2e).

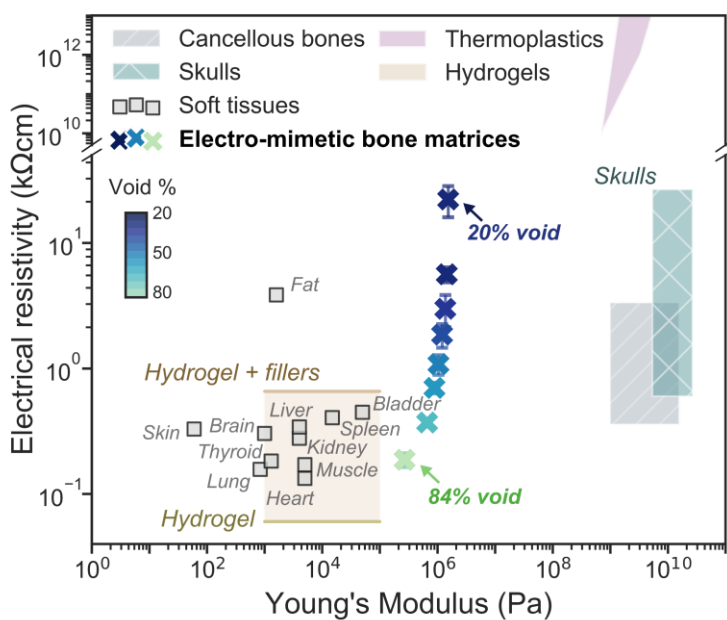
154

155 Fig.3 shows a material property chart summarising the electrical resistivity and the Young's  
156 modulus for a range of biological tissues and polymeric materials. The 3D printed electro-  
157 mimetic bone matrices cover a wide resistivity range, which cannot be imitated by a single  
158 printable material (i.e. thermoplastics or hydrogels) alone or a hydrogel-filler matrix (i.e.  
159 bioceramics and PDMS microbeads dispersed in hydrogels) (Supplementary Fig.4a). Apart  
160 from electrical resistivity, we suggest that Young's modulus of the model is also an important  
161 consideration for electronic implant testing, because the mechanical properties of the  
162 implanted tissues will also determine the final position of the CI electrode array inside the  
163 cochlea. Adopting PDMS as the solid phase of the electro-mimetic bone matrix not only

164 facilitates the ease of embedded printing, but also imparts favourable mechanical properties  
165 as a CI testing platform. With a Young's modulus in the  $10^6$  Pa range, we estimate that the  
166 force associated with CI electrode insertion will not induce a significant deformation to the  
167 matrix (Supplementary Note 1). At the same time, the compliance of the matrix mitigates  
168 mechanical damages to the fine electrodes of a CI, which is commonly experienced when  
169 inserting CI electrode arrays repeatedly in cadaveric samples (modulus of hard tissues  $> 10^9$   
170 Pa). Hence, multiple insertions can take place for the same CI electrode array, which is of  
171 practical importance due to the time-consuming fabrication and costs associated with a CI.  
172 Overall, the above results suggest the electro-mimetic bone matrices to be a suitable material  
173 system for creating electroanatomical models of human cochleae.

174

175 **Fig.3: Wide resistivity tuneability and adequate mechanical properties of electro-**  
176 **mimetic bone matrices.**



177  
178 A map of resistivity versus Young's modulus of human tissues, thermoplastics, the hydrogel-  
179 fillers matrices, and the electro-mimetic bone matrices tested in this study ( $n \geq 3$ ). The  
180 compositions of the hydrogel and hydrogel-filters matrices tested here are listed in  
181 Supplementary Fig.4a. Young's modulus of the electro-mimetic bone matrix was estimated  
182 by scaling the Young's modulus of pure PDMS (1.7 MPa at a curing temperature of 60°C<sup>30</sup>)  
183 linearly with the  $f_{void}$  of the matrix. Tissues and thermoplastics data, and the Young's  
184 modulus of hydrogels were compiled from literature<sup>21,22,35,23–26,31–34</sup>.

185 **3D printed biomimetic cochleae**

186 Clinically, a CI electrode array is inserted into the scala tympani, one of the three cochlear  
187 ducts<sup>13</sup> (Fig.1a). As a coarse-grained approach to replicate the electroanatomical features of a  
188 CI implanted cochlea, we approximate the cochlea as one ensemble spiral cavity with  
189 continuously narrowing diameter, and omit the inner soft-tissue membranous structures of a  
190 cochlea, such as the basilar membrane and Reissner's membrane. This is because, firstly, in a  
191 typical patient's pre-operative CT scan as routine clinical assessment (Fig.1b), the scan  
192 resolution only permits the identification of the shape of the ensemble cochlear lumen and  
193 not the fine microanatomical structures (Supplementary Fig.5); and secondly, our preliminary  
194 finite element modelling shows that the effect of the basilar membrane and the Reissner's  
195 membrane inside a cochlea on the EFI profile at off-stimulation positions is likely to be  
196 insignificant, as the boundary impedances are dominated by surrounding bone tissues (see  
197 Supplementary Fig.6 & 7). Therefore, we constructed the biomimetic cochleae by embedded  
198 3D printing a tapered and spiral-shaped cochlear lumen cavity inside an electro-mimetic bone  
199 matrix (Fig.1c and Supplementary Video 2). The spiral-shaped cavity was filled with a  
200 physiological saline to mimic the ionic conduction milieu in the cochlea (perilymph)  
201 (Supplementary Fig.2c) and the conduction properties at the electrode-electrolyte interface.

202

203 Fig.4a-b show high-resolution micro-CT scans of a cadaveric cochlea and an exemplar 3D  
204 printed biomimetic cochlea with a CI inserted. It is worth noting that the CI electrode-to-  
205 spiral centre distance displayed in the 3D printed cochlea matches closely with the electrode-  
206 to-modiolus distances measured clinically from patients' CT scans<sup>36</sup> (Supplementary Fig.8).  
207 This gives confirmation that the PDMS-based electro-mimetic bone matrix has adequate  
208 structural rigidity to provide geometrically-guided implant insertion and positioning. Since  
209 the size and the shape of a cochlea is unique to an individual and can vary greatly from

210 person-to-person, we assign four geometrical descriptors to numerically describe the reported  
211 anatomical variations in CI implanted human cochleae<sup>37–39</sup>: they are basal lumen diameter,  
212 taper ratio, cochlear width and cochlear height (see definitions in Fig.4c and Supplementary  
213 Table 1). For electroanatomical modelling of cochleae, we incorporated a fifth descriptor, the  
214 matrix resistivity, which is controlled by the void fraction of the electro-mimetic bone matrix.  
215 In total, 82 biomimetic cochleae were printed at different combinations of model descriptors.  
216 With this physical model library, we artificially reconstructed a broad spectrum of the  
217 electroanatomical features of human cochleae with even feature distributions.

218

219 Next, we acquired intracochlear EFI profiles (normalised intracochlear voltage distribution)  
220 in our cochlear models with a CI<sup>1J</sup> (Advanced Bionics HiRes 90K<sup>®</sup> implant with HiFocus<sup>TM</sup>  
221 1J electrode) inserted. EFI samples the intracochlear voltage (V) along the electrode array in  
222 response to a current injection or a stimulation impulse ( $I_{stim}$ ) at each electrode (Fig.1b). The  
223 off-stimulation measurements in EFI profiles contain information about the induced voltage  
224 spread characteristics of the cochlea. EFIs and similar measures (e.g. transimpedance matrix  
225 from Cochlear Corporation<sup>®</sup> or Impedance Field Telemetry from MED-EL<sup>®</sup>) are commonly  
226 used as part of the routine CI clinical assessment.

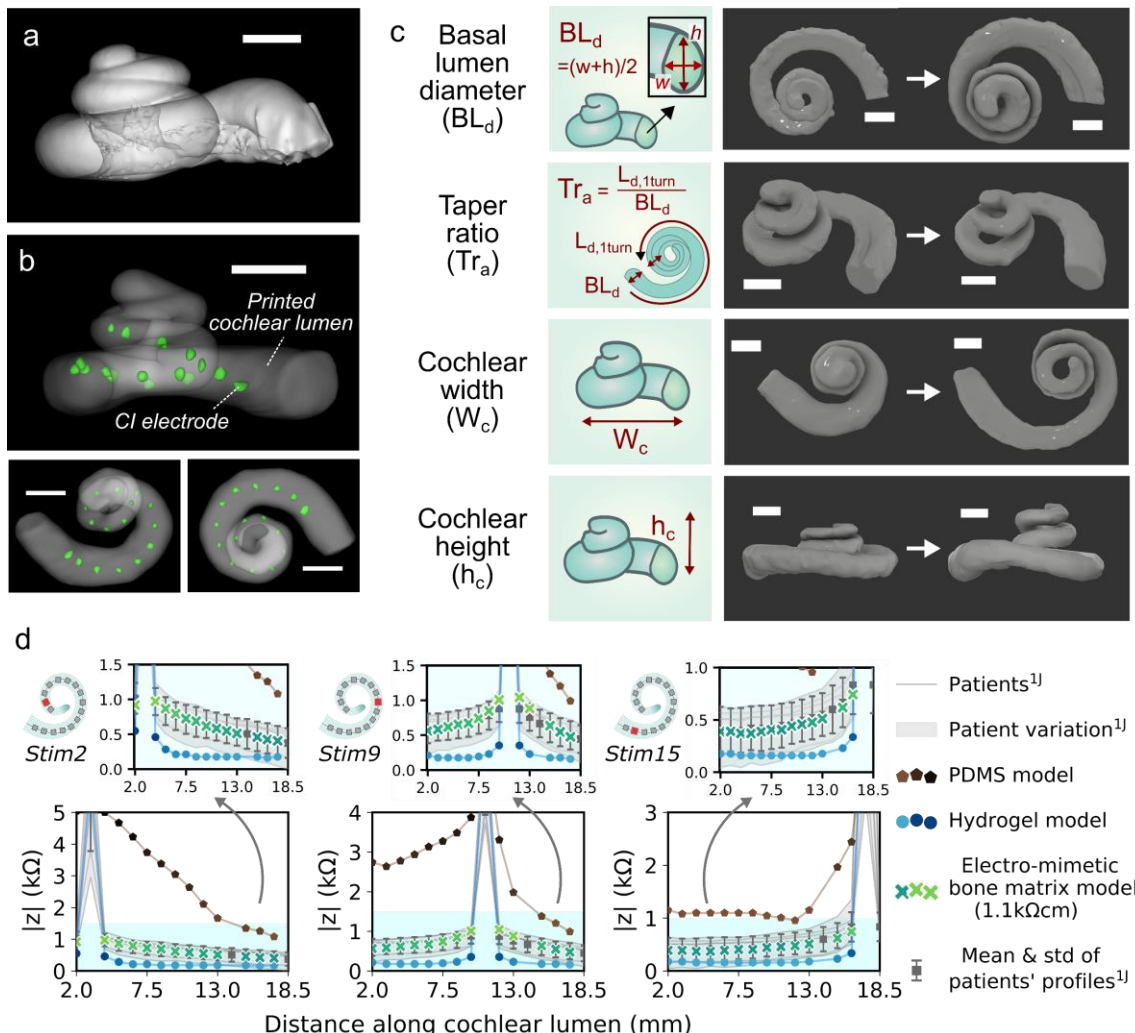
227

228

229

230

231 **Fig.4: 3D printed biomimetic cochleae to replicate the broad anatomical spectrum of**  
232 **human cochleae and give patient-relevant EFI profile.**



233 Micro-CT reconstructed images of (a) a cadaveric cochlea and (b) the lumen of a 3D printed  
234 biomimetic cochlea with CI electrode (marked green) implanted. Scale bar = 2mm. c, Micro-  
235 CT reconstructed images of the spiral cavity of the biomimetic cochlea with different  
236 geometric features. Scale bar = 2mm. Four geometric descriptors are used – basal lumen  
237 diameter, taper ratio, cochlear width, and cochlear height. Detailed definitions and the range  
238 of the descriptors tested in this study can be found in Supplementary Table 1. d, Comparison  
239 of the mean EFI profile of patients implanted with CI<sup>1J</sup> and the EFI profiles obtained from 3D  
240 printed models made of hydrogel, PDMS and electro-mimetic bone matrix. EFI induced by  
241 the stimulations of the apical electrode (electrode 2), the medial electrode (electrode 9) and  
242 the basal electrode (electrode15) were shown.

244  
245 To further demonstrate the importance of having a realistic bone matrix resistivity in  
246 reproducing the patient EFI profile, we also fabricated models made of materials with

247 contrasting conduction properties, hydrogels (representing the highly conductive case) and  
248 solid PDMS (representing the insulating case). Fig.4d shows the mean patient's EFI profile  
249 derived from 6 patients implanted with an Advanced Bionics CI<sup>1J</sup> compared with the EFI  
250 profiles of the 3D printed models. We found that the PDMS model led to a steeper and  
251 extremely asymmetrical EFI profile (as seen in the stimulation at the medial electrode),  
252 strongly mismatched with patient profiles. In comparison, the conductive hydrogel  
253 model resulted in a low magnitude EFI profile. By replicating realistic bone resistivities with  
254 electro-mimetic bone matrices, our biomimetic cochlea can be designed to match the  
255 patient's stimulus spread characteristics.

256 **Clinically validated 3PNN shows high predictive performance**

257 By training a neural network (NN) model with the EFI profiles acquired from the 3D printed  
258 biomimetic cochleae, a 3D printing and neural network co-modelling (3PNN) framework  
259 (Fig.5a) was established to model the relationship between EFIs and the electroanatomical  
260 features of the CI implanted biomimetic cochleae. Reasons for using NN modelling instead  
261 of other existing computational models are discussed in Supplementary Note 2 and  
262 Supplementary Fig.10. To support various application needs, we developed forward-3PNN  
263 and inverse-3PNN. Forward-3PNN is used to predict EFIs arising from different  
264 electroanatomical descriptors of a cochlea, coupled with different CI stimulus and recording  
265 positions (covering 18.5mm section of a CI from different manufacturers that may have  
266 different electrode locations and spacings). Inverse-3PNN has the ability to infer the  
267 distribution of the electroanatomical descriptors of a cochlea for a given EFI profile.

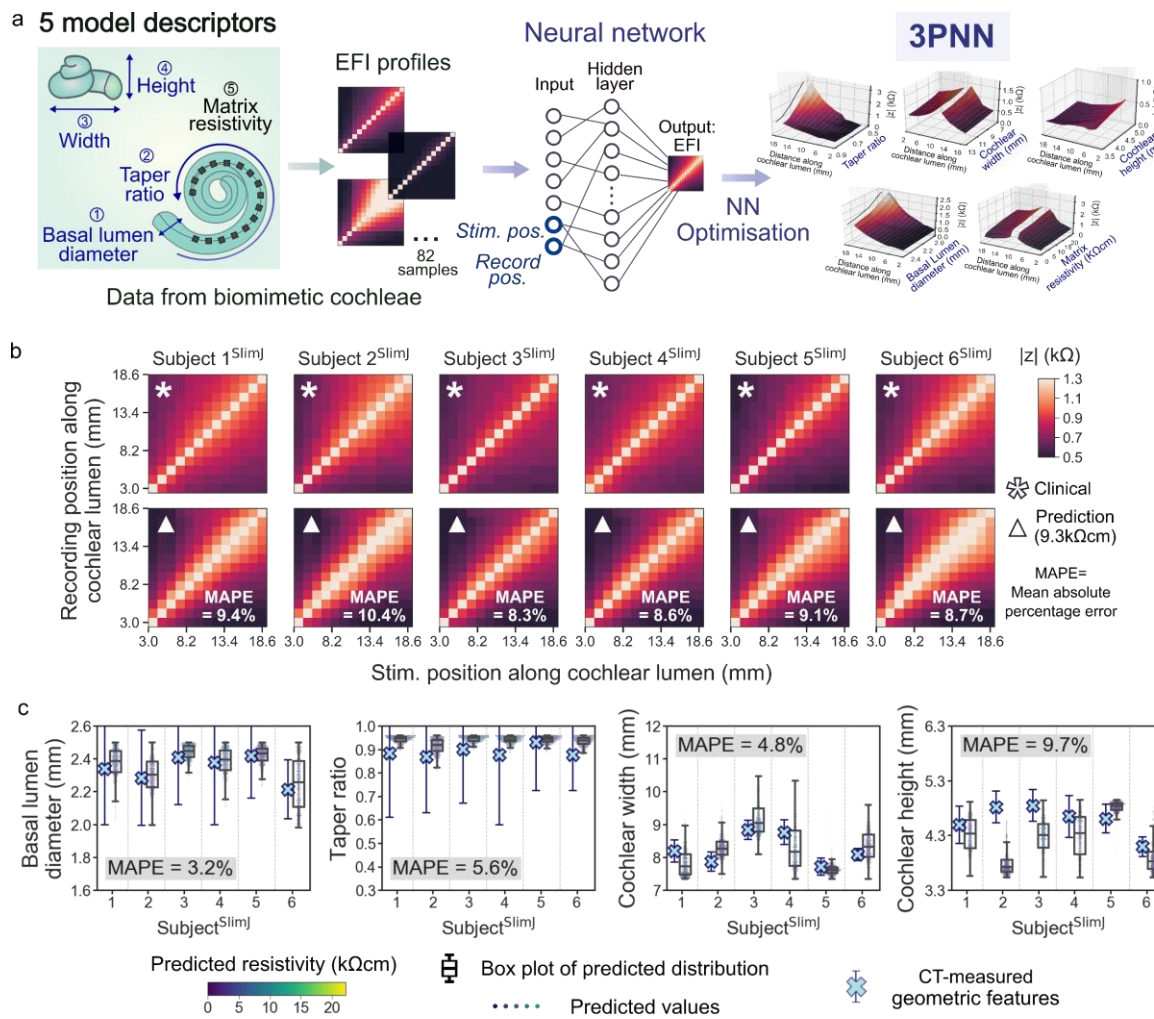
268

269 We validated the clinical applicability of 3PNN using routinely acquired clinical data. In  
270 total, six paired sets of patient's CT scan and EFI profile acquired with a lateral wall CI

271 (HiRes<sup>TM</sup> Ultra HiFocus<sup>TM</sup> SlimJ electrode array, CI<sup>SlimJ</sup>) were used for validation, an  
272 electrode similar to the model test electrode , CI<sup>1J</sup>. Starting with our forward-3PNN, we  
273 predicted patients' EFI profiles at off-stimulation positions based on the four geometric  
274 descriptors measured from their CT scans, while assuming the matrix resistivity inputs are  
275 equal to a default value of 9.3kΩcm (which is the mean reported resistivity of live human  
276 skulls obtained during surgery<sup>21–25</sup>, see Supplementary Fig.1a). The predicted off-stimulation  
277 EFI profiles (EFI arising from off stimulation positions) match the patients' clinical profiles  
278 with a 10% MAPE (mean absolute percentage error) (Fig.5b), considering the limited  
279 resolution of patients' cochlear CT scans, and the non-patient specific cochlear resistivity.  
280  
281 We further validated our 3PNN by inversely inferring the distribution of the model  
282 descriptors that could match a patient's off-stimulation EFI profile with an average similarity  
283 over 92%. Comparing the predicted distributions of the four geometric descriptors with the  
284 corresponding patient's features measured from their CT scans, MAPE is less than 10%  
285 (Fig.5c). Nevertheless, the predictive quality in cochlear height is less satisfactory compared  
286 to the predictions of basal lumen diameter, taper ratio, and cochlear width, which closely  
287 match the measured patients' features with MAPE less than 6%.

288

289 **Fig.5: Clinical Validation of 3PNN.**



290

291 **a**, Schematic of the workflow of 3PNN. 3PNN was developed by training a neural network  
292 model with the EFI profiles acquired from the 3D printed biomimetic cochleae. 3PNN  
293 models the mapping from the 5 model descriptors, the stimulus position and the recording  
294 position to the EFI profile. The hyperparameters of 3PNN were tuned using 10-fold cross-  
295 validation to achieve the best predictive performance (Supplementary Fig.11). **b**, Validation  
296 of the forward-3PNN by comparing the patients' clinical EFI profiles with the predicted EFI  
297 profiles derived from the geometric descriptors of patients' cochlear CTs at off-stimulation  
298 positions. The matrix resistivity inputs were defaulted as the mean reported resistivity of live  
299 human skulls (9.3kΩcm). MAPE (mean absolute percentage error) is used to quantify the  
300 predictive performance. **c**, Validation of the inverse-3PNN by comparing the patient's  
301 geometric descriptors measured from their cochlear CT scans with the predicted distribution  
302 of the geometric descriptors that could result in an off-stimulation EFI profile with an  
303 average similarity over 92% to the patient's profile. To approximate the predicted distribution  
304 of the descriptors, 1000 predicted sets of the model descriptors were plotted for each  
305 predicted distribution, and the distribution is depicted by a box plot. Colour of each point  
306 denotes the predicted resistivity. Error bars of the patients' CT-measured geometric features  
307 were approximated as 1 pixel size of the CT scans.

308 **Effect of cochlear electroanatomy on CI voltage spread**

309 With the validated 3PNN model, we proceeded to investigate how the CI voltage spread  
310 characteristics could be affected by the four geometric descriptors and the matrix resistivity.  
311 Using forward-3PNN, we simulated EFI profiles by sweeping through different combinations  
312 of the 5 model descriptors (examples shown in Supplementary Fig.12). To parameterise the  
313 voltage spread characteristics shown in the EFI profiles, we fitted a power law, Equation (1),  
314 to each stimulus spread toward the apex and toward the base (detailed examples shown in  
315 Supplementary Fig.13).

$$|z| = \frac{V}{I_{stim}} = Ax^{-b} \quad (1)$$

316 where  $|z|$  = transimpedance magnitude,  $V$  = voltage between the recording electrode and the  
317 ground electrode,  $I_{stim}$  = stimulation impulse current,  $x$  = distance along the cochlear lumen  
318 from the stimulating electrode,  $A$  = baseline coefficient and  $b$  = coefficient indicating how  
319 fast voltage drops over a distance. The larger the  $b$  value, the sharper the voltage drop. The  
320 power law relation was adopted here because, theoretically, volume conduction from a point  
321 source in a homogeneous medium should follow an inverse relationship with the form of  
322  $|z| = \frac{1}{4\pi\sigma r}$ , where  $\sigma$  = conductivity of the homogeneous medium and  $r$  = distance from the  
323 stimulating electrode<sup>40</sup>. The mean fitting coefficients ( $\bar{A}_{apex}$ , and  $\bar{A}_{base}$ ) were used here to  
324 quantify the mean baseline coefficient; and  $\bar{b}_{apex}$  and  $\bar{b}_{base}$  were used as indicators of the  
325 sharpness of voltage drop toward the apex and the base of the cochlea.

326

327 As evidenced in Supplementary Fig.14, we confirm that the trend of the magnitude of EFI  
328 across each descriptor is independent of other model descriptors. Therefore, we examined the  
329 dependence of the mean coefficients  $\bar{A}$  and  $\bar{b}$  across each model descriptor individually

330 (Fig.6a). We found that both the geometric descriptors and the matrix resistivity affect the  
331 mean baseline coefficient  $\bar{A}$ , whilst the matrix resistivity in the range we investigated does  
332 not seem to play a key role in the voltage drop coefficient,  $\bar{b}$ . In addition, our findings  
333 suggest that the voltage drop is shallower (smaller  $\bar{b}$  value) in the following scenarios:  
334 cochleae with larger basal lumen diameter, less tapered cochlear lumen (i.e. taper ratio closer  
335 to 1) and smaller cochlear width. Therefore, we expect that cochleae with these geometric  
336 features have more intracochlear voltage spread, which may activate a larger number of  
337 neurones over a broader region. However, the activation function for neurones should also be  
338 considered for a more sophisticated prediction of the activation of neurons<sup>41</sup>.

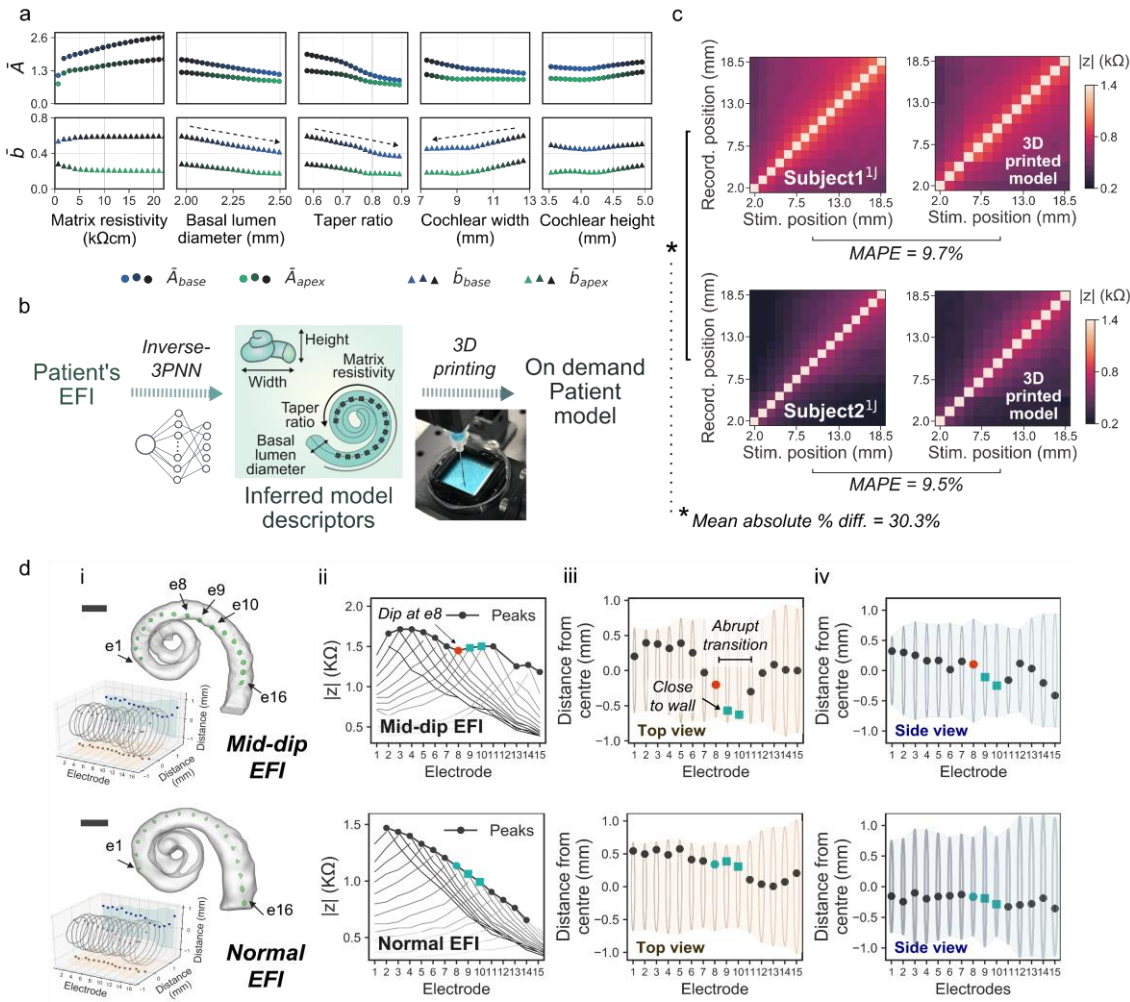
339

#### 340 **On-demand creation of biomimetic cochleae inheriting patient EFIs**

341 The clinical validation of 3PNN demonstrates that the 3D printed cochleae can reproduce the  
342 off-stimulation EFIs of CI users with high fidelity, despite the physical simplicity of the  
343 models. With such a validated platform, we further demonstrate its application to construct  
344 on-demand biomimetic cochleae that can yield patient-specific off-stimulation EFI profiles.  
345 To do this, we first used the inverse-3PNN to obtain the distribution of the model descriptors  
346 that could match each patient's off-stimulation EFI profile with an average similarity over  
347 90% (Fig.6b and Supplementary Fig.15). Subsequently, embedded 3D printing was used to  
348 fabricate a patient-specific biomimetic cochlea exhibiting the features of a set of model  
349 descriptors inferred from inverse-3PNN. As shown in Fig.6c, the EFI profiles measured from  
350 the 3D printed biomimetic cochleae show good resemblance to their corresponding patients'  
351 off-stimulation EFI profiles, with MAPE less than 10%; while the patients' EFI profiles show  
352 a dissimilarity of over 30% MAPE.

353

354 **Fig.6: Broad applicability of 3PNN for clinical informatics.**



355

356 **a**, The trend of the mean baseline coefficient ( $\bar{A}_{\text{apex}}, \bar{A}_{\text{base}}$ ), and the indicators of the sharpness  
357 of voltage drop ( $\bar{b}_{\text{apex}}, \bar{b}_{\text{base}}$ ) toward the apex and toward the base of the cochlea across each  
358 model descriptor. The arrow direction indicates the decreasing sharpness of voltage drop in  
359 these cochlear features, which suggests an increased voltage spread susceptibility. **b**,  
360 Schematic showing the process to generate the patient-specific biomimetic cochlea, where  
361 inverse-3PNN was used to deduce the model descriptors best-fitting the patient off-  
362 stimulation EPI, and the patient cochlear model was then fabricated by 3D printing with one  
363 of the predicted sets of the model descriptors (Supplementary Fig.15). **c**, Comparison of the  
364 off-stimulation EFIs of two patients and the off-stimulation EFIs acquired in their  
365 corresponding biomimetic cochleae. The model descriptors used to produce the biomimetic  
366 cochleae of subject1<sup>1J</sup> and subject2<sup>1J</sup> are as follows: matrix resistivity 2.9 versus 0.7k $\Omega\text{cm}$ ,  
367 and taper ratio 0.9 versus 0.7, respectively, while with similar basal lumen diameter~2.4mm,  
368 cochlear width~10.5mm, and cochlear height~4.4mm. **d**, The electrode positions in a model  
369 showing an uncommon ‘mid-dip’ EPI profile (top) and a model with a typical EPI profile  
370 (bottom). **(i)** Reconstructed 3D micro-CT volumes of the cochlear lumens of the biomimetic  
371 cochleae with a CI electrode array inserted (marked green); **(ii)** EPI profiles of the models;  
372 **(iii)** Top view and **(iv)** side view of the cochlear lumens of the models, showing the positions  
373 of the electrodes in the models relative to the lumen wall.

374 Beyond the application of reproducing patient-specific EFI profile with a physical 3D printed  
375 model, our platform further points to the potential occurrence of uncommon EFI profiles,  
376 such as the ‘mid-dip’ characteristics occasionally observed in patients. The ‘mid-dip’  
377 characteristic (Fig.6d), which is distinguished by a dip in the EFI profile at the medial  
378 electrodes, has not been given a clear clinical explanation. It is uncertain whether  
379 implantation abnormality or patient-specific cochlear biologic properties could be the origin.  
380 By visualising the positions of electrodes in our 3D printed models with micro-CT imaging,  
381 we found that the electrode position, which was guided by the cochlear geometry, could be a  
382 potential explanation. As shown in Fig.6d, the mid-dip characteristics can be produced by a  
383 specific combination of cochlear shape and CI positioning. In the model with the ‘mid-dip’  
384 characteristics, the electrode positions appear to change abruptly (panel iii in Fig.6d), where  
385 electrode 8 (e8) was adjacent to two ‘near-wall’ electrodes (e9 and e10) that were in close  
386 proximity to the spiral centre (Supplementary Fig.8). This sudden decrease in the electrode-  
387 to-wall distance can potentially cause a slight increase in the EFI profile, hence a dip at e8 in  
388 the profile. On the contrary, in the model without the ‘mid-dip’ characteristics, the electrode  
389 positions changed gradually. This suggests that the relative position of the electrode to the  
390 neighbouring electrodes and the lumen wall can be one of the factors of the mid-dip  
391 abnormality in the EFI profile.

392

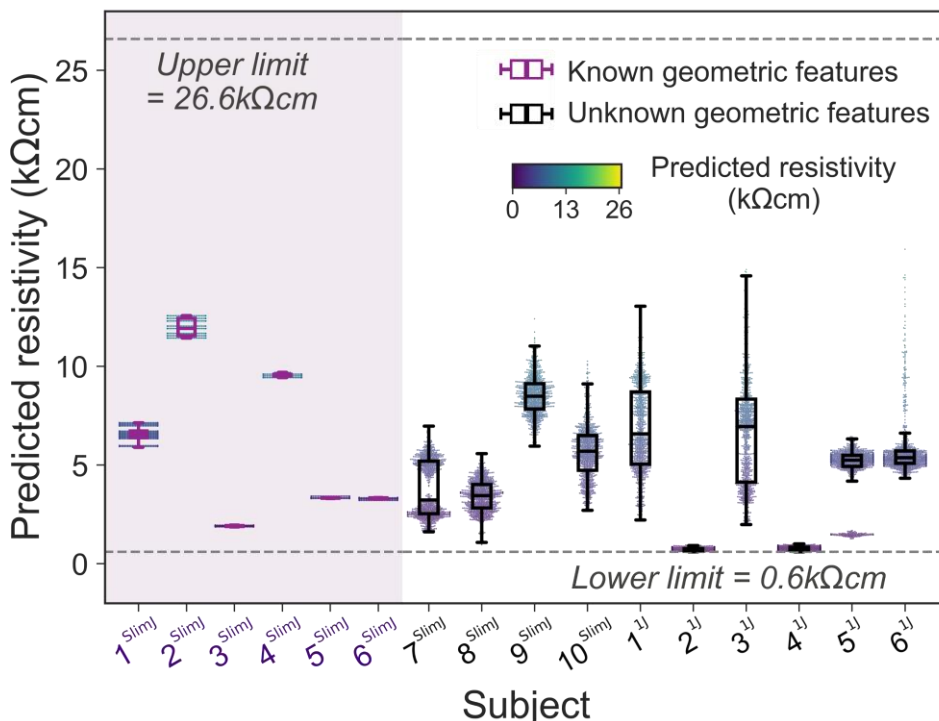
### 393 **Informing patient-specific cochlear tissue resistivity**

394 As the absolute resistivity of patients’ temporal bones near the cochlear vicinity cannot be  
395 measured non-invasively in living subjects, our inverse-3PNN further presents a unique  
396 capability of deducing the resistivities of patients’ cochlear tissues based on their individual  
397 EFI profiles. 16 patients implanted with CI<sup>SlimJ</sup> or CI<sup>1J</sup> were examined here. Fig.7 shows the  
398 ranges of the patient-specific resistivities, which were deduced with paired pre-op CT (thus

399 known patient geometric descriptors) for subjects<sup>SlimJ</sup> 1-6 and with unknown geometric  
400 descriptors for the rest. The predictions were undertaken with the criterion that the off-  
401 stimulation EFI profiles simulated from the inferred sets of the model descriptors are less  
402 than 10% MAPE to the patient's profile.

403

404 **Fig.7: 3PNN informing patient-specific resistivity of the cochlear tissue.**



405

406 Predictions of subjects 1-6<sup>SlimJ</sup> were carried out with known patient's geometric descriptors  
407 measured from their cochlear CT scans, whereas predictions of subjects 7-10<sup>SlimJ</sup> and subjects  
408 1-6<sup>J</sup> were undertaken where patient's geometric descriptors were unavailable due to  
409 restricted access to the patient CT scans. Dotted lines show the reported upper and lower  
410 limits of *in vivo* human skull resistivities<sup>21-25</sup>.

411

412 All the predicted patient resistivity ranges (0.6 – 15.9 kΩcm) lie within the reported  
413 resistivity range (0.6 – 26.6 kΩcm) of live human skulls measured during intra-operative  
414 procedures<sup>21-25</sup>. In particular, the predicted resistivity ranges are at the lower end of the full  
415 reported range of cortical bone/skull resistivities (i.e. 0.4 – 84 kΩcm which encompasses

416 animal, cadaver and living human measurements)<sup>10,21,45,46,22–26,42–44</sup>. With known values of  
417 patient geometric descriptors, which can be obtained from patients' standard-of-care CT  
418 scans, the predictions of patient-specific cochlear bone resistivities achieve a much smaller  
419 uncertainty, with a relative standard deviation less than 5%. Thus, our methodology could  
420 provide a method to readily deduce the *in vivo* bulk resistivity of individual patient's cochlear  
421 bone matrix via CI telemetry. This could be useful in monitoring otic bone demineralization  
422 conditions such as otosclerosis in future work.

423

## 424 Discussion

425 We created a physical library of 3D printed biomimetic cochlear models, which closely  
426 captures the reported broad spectrum of EFI profiles of CI patients at off-stimulation  
427 positions that describes the electrical conduction through tissues<sup>9</sup>. 3D printed cochlear  
428 models were designed with resistivity-tunable electro-mimetic bone matrices. These  
429 physical models displayed suitable mechanical stiffness for geometrically-guided CI  
430 insertion, while limiting damage to CI electrodes during insertion. It is noted that the  
431 biomimetic cochleae did not account for the frictional force generated during CI insertions  
432 under the basilar membrane in human cochleae, which may cause electrode array buckling or  
433 even intracochlear trauma affecting CI performance<sup>47,48</sup>. We suggest that friction could have  
434 attributed to the localised buckling configuration of the CI electrode array captured in the 3D  
435 model giving the 'mid-dip' EFI.

436

437 Our neural network model trained by measurements of 3D printed biomimetic cochleae  
438 (3PNN) constitutes a simple 5-parameter model that can readily extract data and information  
439 from CI patients under established clinical procedures. The potential broad and non-case  
440 specific applicability of 3PNN is demonstrated by the fact that the neural network was trained

441 by experimental EFIs measured by CI<sup>1J</sup>, but off-stimulation EFIs of patients implanted with  
442 CI<sup>SlimJ</sup> (up to a position of 18.5 mm along the cochlear lumen) can be successfully inferred  
443 without further model adjustment and re-calibration. Therefore, the framework has a potential  
444 capability of forecasting the post-operative electrical performances of CIs from different  
445 manufacturers, hence assisting the development of CIs tailored to patient anatomy.

446 Comparing to conventional animal and cadaver models, the ‘print-and-learn’ concept  
447 proposed here offers a physical-manipulatable, ethical and economic approach, which may  
448 help reduce the need for animal experiments and, at the same time, provide a sufficient  
449 statistical predictive power for preliminary CI testing.

450

451 The 3D printed biomimetic cochleae offer a robust physical means to capture the variability  
452 in anatomical-guided CI insertion, and replicate the ionic conduction and the electron-ion  
453 interaction in cochleae with implanted CIs. The 3PNN framework could provide an important  
454 tool for solving the ‘volume conduction’ problem, the first step in computational  
455 neuroengineering for modelling electrical stimulation in a biological structure<sup>19</sup>. Further  
456 studies that evaluate the correlation between the intracochlear voltage distribution and the  
457 excitation of neural cells will be of particular benefit to expand the use of 3PNN in modelling  
458 the excitation spread at the neuronal level.

459

460 The ability of 3PNN to deduce patient-specific *in vivo* resistivity of the cochlear tissue by CI  
461 telemetry provides a valuable reference for cochlear bioelectric research. We anticipate that  
462 this unique capability might enable long-term monitoring of patients’ cochlear health after CI  
463 implantation. For example, it has been suggested that the electrical properties of cochlear  
464 tissues can be affected by a variety of physiological and otologic diseases, such as post-  
465 implantation fibrosis and neo-ossification, post-operative electrode extrusion and

466 medications<sup>13,49,50</sup>. Hence, the cochlear tissue resistivities informed by patients' EFI profiles  
467 might be used as a diagnostic indicator to detect early abnormalities, without resorting to  
468 ionizing radiation of patients (which particularly should be avoided in children). With the  
469 rising usage of neuromodulating electronic implants, we anticipate that our 'print-and-learn'  
470 electroanatomical framework could facilitate the optimisation process and the pre-clinical  
471 screening of bioelectronic implant prototypes, beyond its applications in CIs.

472

473 **References**

- 474 1. Schiavone, G. & Lacour, S. P. Conformable bioelectronic interfaces: Mapping the road  
475 ahead. *Sci. Transl. Med.* (2019).
- 476 2. Birmingham, K. *et al.* Bioelectronic medicines: A research roadmap. *Nature Reviews  
477 Drug Discovery* vol. 13 399–400 (2014).
- 478 3. Famm, K., Litt, B., Tracey, K. J., Boyden, E. S. & Slaoui, M. A jump-start for  
479 electroceuticals. *Nature* (2013).
- 480 4. Dieter, A., Duque-Afonso, C. J., Rankovic, V., Jeschke, M. & Moser, T. Near  
481 physiological spectral selectivity of cochlear optogenetics. *Nat. Commun.* (2019).
- 482 5. Macherey, O. & Carlyon, R. P. Cochlear implants. *Current Biology* (2014).
- 483 6. Drennan, W. R., Svirsky, M. A., Fitzgerald, M. B. & Rubinstein, J. T. Mimicking  
484 Normal Auditory Functions with Cochlear Implant Sound Processing : Past, Present,  
485 and Future. in *Cochlear Implants* (eds. Waltzman, S. B. & Roland, J. T.) 47–60  
486 (Thieme Medical Publishers, Incorporated, 2014).
- 487 7. Ben-Menachem, E. Vagus-nerve stimulation for the treatment of epilepsy. *Lancet  
488 Neurology* (2002).
- 489 8. Vöröslakos, M. *et al.* Direct effects of transcranial electric stimulation on brain circuits  
490 in rats and humans. *Nat. Commun.* (2018).
- 491 9. Vanpoucke, F. J., Zarowski, A. J. & Peeters, S. A. Identification of the impedance  
492 model of an implanted cochlear prosthesis from intracochlear potential measurements.  
493 *IEEE Trans. Biomed. Eng.* (2004).
- 494 10. Frijns, J. H. M., de Snoo, S. L. & Schoonhoven, R. Potential distributions and neural  
495 excitation patterns in a rotationally symmetric model of the electrically stimulated

- 496 cochlea. *Hear. Res.* (1995).

497 11. Shepherd, R. K., Hatsushika, S. & Clark, G. M. Electrical stimulation of the auditory  
498 nerve: The effect of electrode position on neural excitation. *Hear. Res.* (1993).

499 12. Nogueira, W., Schurzig, D., Büchner, D., Penninger, R. T. & Würfel, W. Validation of  
500 a cochlear implant patient-specific model of the voltage distribution in a clinical  
501 setting. *Front. Bioeng. Biotechnol.* (2016).

502 13. Maura K. Cosetti. Intraoperative Monitoring During Cochlear Implantation. in  
503 *Cochlear Implants* (eds. Susan B. Waltzman & J. Thomas Roland) 100–107 (Thieme  
504 Medical Publishers, Incorporated, 2014).

505 14. Wong, P. *et al.* Development and validation of a high-fidelity finite-element model of  
506 monopolar stimulation in the implanted Guinea pig cochlea. *IEEE Trans. Biomed.  
507 Eng.* (2016).

508 15. Adunka, O., Kiefer, J., Unkelbach, M. H., Lehnert, T. & Gstoettner, W. Development  
509 and evaluation of an improved cochlear implant electrode design for electric acoustic  
510 stimulation. *Laryngoscope* (2004).

511 16. Huang, C. Q., Shepherd, R. K., Carter, P. M., Seligman, P. M. & Tabor, B. Electrical  
512 stimulation of the auditory nerve: Direct current measurement in vivo. *IEEE Trans.  
513 Biomed. Eng.* (1999).

514 17. Ekdale, E. G. Form and function of the mammalian inner ear. *J. Anat.* (2016).

515 18. Opitz, A., Falchier, A., Linn, G. S., Milham, M. P. & Schroeder, C. E. Limitations of  
516 ex vivo measurements for in vivo neuroscience. *Proc. Natl. Acad. Sci. U. S. A.* (2017).

517 19. Romeni, S., Valle, G., Mazzoni, A. & Micera, S. Tutorial: a computational framework  
518 for the design and optimization of peripheral neural interfaces. *Nat. Protoc.* **15**, 3129–  
519 3153 (2020).

520 20. Malherbe, T. K., Hanekom, T. & Hanekom, J. J. The effect of the resistive properties  
521 of bone on neural excitation and electric fields in cochlear implant models. *Hear. Res.*  
522 (2015).

523 21. Tang, C. *et al.* Correlation between structure and resistivity variations of the live  
524 human skull. *IEEE Trans. Biomed. Eng.* (2008).

525 22. Akhtari, M. *et al.* Conductivities of three-layer live human skull. *Brain Topogr.*  
526 (2002).

527 23. Hoekema, R. *et al.* Measurement of the conductivity of skull, temporarily removed  
528 during epilepsy surgery. *Brain Topogr.* (2003).

529 24. Oostendorp, T. F., Delbeke, J. & Stegeman, D. F. The conductivity of the human skull:

- 530                  Results of in vivo and in vitro measurements. *IEEE Trans. Biomed. Eng.* (2000).
- 531    25. Charles C. Finley, Wilson, B. S. & Mark W. White. Models of Neural Responsiveness  
532                  to Electrical Stimulation. in *Cochlear Implants : Models of the Electrically Stimulated*  
533                  *Ear* (eds. Josef M. Miller & Francis A. Spelman) 55–96 (Springer, 1990).
- 534    26. Balmer, T. W., Vesztergom, S., Broekmann, P., Stahel, A. & Büchler, P.  
535                  Characterization of the electrical conductivity of bone and its correlation to osseous  
536                  structure. *Sci. Rep.* (2018).
- 537    27. Kolesky, D. B. *et al.* 3D bioprinting of vascularized, heterogeneous cell-laden tissue  
538                  constructs. *Adv. Mater.* (2014).
- 539    28. Advanced Bionics. *HiRes 90K® Surgeon's Manual for the HiFocus® Helix and*  
540                  *HiFocus® 1j Electrodes*. (2005).
- 541    29. Armin Bunde & Jan W. Kantelhardt. Diffusion and Conduction in Percolation Systems  
542                  – Theory and Applications. in *Diffusion in Condensed Matter* (eds. Heitjans, P. & Jörg  
543                  Kärger) 895–914 (Springer, 2005).
- 544    30. Johnston, I. D., McCluskey, D. K., Tan, C. K. L. & Tracey, M. C. Mechanical  
545                  characterization of bulk Sylgard 184 for microfluidics and microengineering. *J.*  
546                  *Micromechanics Microengineering* (2014).
- 547    31. Faes, T. J. C., Van Der Meij, H. A., De Munck, J. C. & Heethaar, R. M. The electric  
548                  resistivity of human tissues (100 HZ-10 MHZ): A meta- analysis of review studies.  
549                  *Physiological Measurement* (1999).
- 550    32. Guimarães, C. F., Gasperini, L., Marques, A. P. & Reis, R. L. The stiffness of living  
551                  tissues and its implications for tissue engineering. *Nature Reviews Materials* (2020).
- 552    33. Rho, J. Y., Tsui, T. Y. & Pharr, G. M. Elastic properties of human cortical and  
553                  trabecular lamellar bone measured by nanoindentation. *Biomaterials* (1997).
- 554    34. Yang, C. & Suo, Z. Hydrogel ionotronics. *Nature Reviews Materials* (2018).
- 555    35. A J Pearmain & A G Clegg. Insulators. in *Electrical Engineer's Reference Book* (ed. G  
556                  R Jones) 15 (Elsevier Ltd, 2013).
- 557    36. Davis, T. J. *et al.* Relationship between electrode-to-modiolus distance and current  
558                  levels for adults with cochlear implants. *Otol. Neurotol.* (2016).
- 559    37. Erixon, E., Högstorp, H., Wadin, K. & Rask-Andersen, H. Variational anatomy of the  
560                  human cochlea: Implications for cochlear implantation. *Otol. Neurotol.* (2009).
- 561    38. Pelliccia, P. *et al.* Cochlea size variability and implications in clinical practice. *Acta*  
562                  *Otorhinolaryngol. Ital.* (2014).
- 563    39. Mori, M. C. & Chang, K. W. CT analysis demonstrates that cochlear height does not

- 564 change with age. *Am. J. Neuroradiol.* (2012).
- 565 40. Horch, K. W. & Burgess, P. R. Peripheral Nervous System. in *Neuroprosthetics: Theory and Practice* (eds. Kenneth W. Horch & Gurpreet S. Dhillon) 30–45 (World Scientific Publishing Co.Pte. Ltd., 2004).
- 566 41. Rattay, F. The basic mechanism for the electrical stimulation of the nervous system. *Neuroscience* (1999).
- 567 42. Akhtari, M. *et al.* Conductivities of three-layer human skull. *Brain Topogr.* (2000).
- 568 43. Law, S. K. Thickness and resistivity variations over the upper surface of the human skull. *Brain Topogr.* (1993).
- 569 44. Saha, S. & Williams, P. A. Electric and Dielectric Properties of Wet Human Cortical Bone as a Function of Frequency. *IEEE Trans. Biomed. Eng.* (1992).
- 570 45. Micco, A. G. & Richter, C. P. Electrical resistivity measurements in the mammalian cochlea after neural degeneration. *Laryngoscope* (2006).
- 571 46. Briaire, J. J. & Frijns, J. H. M. Field patterns in a 3D tapered spiral model of the electrically stimulated cochlea. *Hear. Res.* (2000).
- 572 47. Todd, C. A., Naghdy, F. & Svehla, M. J. Force application during cochlear implant insertion: An analysis for improvement of surgeon technique. *IEEE Trans. Biomed. Eng.* (2007).
- 573 48. Zeng, F. G., Rebscher, S., Harrison, W., Sun, X. & Feng, H. Cochlear Implants: System Design, Integration, and Evaluation. *IEEE Rev. Biomed. Eng.* (2008).
- 574 49. Frijns, J. H. M., Kalkman, R. K. & Briaire, J. J. Stimulation of the facial nerve by intracochlear electrodes in otosclerosis: A computer modeling study. *Otol. Neurotol.* (2009).
- 575 50. Carré, F., Achard, S., Rouillon, I., Parodi, M. & Loundon, N. Hearing impairment and osteogenesis imperfecta: Literature review. *European Annals of Otorhinolaryngology, Head and Neck Diseases* (2019).
- 576 51. Pietsch, M. *et al.* Spiral Form of the Human Cochlea Results from Spatial Constraints. *Sci. Rep.* (2017).
- 577 52. Jiang, C., de Rijk, S. R., Malliaras, G. G. & Bance, M. L. Electrochemical impedance spectroscopy of human cochleas for modeling cochlear implant electrical stimulus spread. *APL Mater.* **8**, 1–8 (2020).
- 578 53. Fedorov, A. *et al.* 3D Slicer as an image computing platform for the Quantitative Imaging Network. *Magn. Reson. Imaging* (2012).
- 579 54. Hornik, K., Stinchcombe, M. & White, H. Multilayer feedforward networks are

- 598 universal approximators. *Neural Networks* (1989).
- 599 55. Abadi, M. *et al.* TensorFlow: A system for large-scale machine learning. in  
600 *Proceedings of the 12th USENIX Symposium on Operating Systems Design and*  
601 *Implementation, OSDI 2016* (2016).
- 602 56. Kingma, D. P. & Ba, J. L. Adam: A method for stochastic optimization. in *3rd*  
603 *International Conference on Learning Representations, ICLR 2015 - Conference*  
604 *Track Proceedings* (2015).
- 605 57. Kohavi, R. A Study of Cross-Validation and Bootstrap for Accuracy Estimation and  
606 Model Selection. *Int. Jt. Conf. Artif. Intell.* (1995).
- 607 58. Toni, T., Welch, D., Strelkowa, N., Ipsen, A. & Stumpf, M. P. H. Approximate  
608 Bayesian computation scheme for parameter inference and model selection in  
609 dynamical systems. *J. R. Soc. Interface* (2009).
- 610 59. Clerx, M. *et al.* Probabilistic Inference on Noisy Time Series (PINTS). *J. Open Res.*  
611 *Softw.* **7**, 23 (2019).
- 612 60. Advanced Bionics. *Surgeon Manual for the HiRes<sup>TM</sup> Ultra Cochlear Implant with the*  
613 *HiFocus<sup>TM</sup> SlimJ and HiFocus<sup>TM</sup> Mid-Scala Electrodes*. (2016).
- 614

615 **Acknowledgements**

616 This work was supported by the European Research Council (ERC-StG, 758865), the  
617 Cambridge Hearing Trust and the Evelyn Trust. I.M.L. acknowledges the financial support  
618 from the W D Armstrong Trust. C.J. acknowledges the support from the Wellcome Trust.  
619 C.L.L. acknowledges the financial support from the Clarendon Scholarship Fund. S.R.D.R.  
620 acknowledges the financial support from the Baroness de Turckheim Fund, Trinity College  
621 Cambridge. We thank Advanced Bionics Corporation® for providing cochlear implants and  
622 software on this research, Anthony Dennis for technical assistance with micro-CT imaging  
623 and Tomasz Matyz for his help with the anonymised patients' CT scans.

624

625 **Author contributions**

626 I.M.L., C.J., M.B. and Y.Y.S.H. conceived the project. I.M.L. performed majority of the  
627 experiments and data analysis including 3D printing and creation of biomimetic cochlear EFI

628 library. C.J. performed the EIS experiments. C.L.L. developed the neural network model and  
629 assisted with part of the data analysis. I.M.L. performed the neural network model  
630 optimisation and simulations. C.J., S.R.D.R., Y.C.T. and M.B. assisted with the anonymised  
631 patient's data collection. Y.Y.S.H., G.G. and M.B. provided result interpretation. M.P.F.S.  
632 performed the mechanical deformation analysis. I.M.L. and Y.Y.S.H. wrote the initial  
633 manuscript. Y.Y.S.H and M.B. supervised the project. All authors discussed the results and  
634 revised the manuscript.

635

### 636 **Competing interests**

637 M.B. received research funding from Advanced Bionics®, Cochlear Corporation®, and in-  
638 kind contribution from MED-EL® on other research areas but not on the present study. The  
639 remaining authors declare no competing interests.